

Enhanced drainage and thinning of liquid films between bubbles and solids that support surface waves

Amihai Horesh, Matvey Morozov, and Ofer Manor*

Department of Chemical Engineering, Technion—Israel Institute of Technology, 32000 Haifa, Israel

(Received 23 February 2017; revised manuscript received 26 April 2017; published 22 May 2017)

We study the thinning and drainage of the intermediate liquid film between a bubble and a solid surface at close proximity in the presence of a surface acoustic wave (SAW) in the solid. Specifically, we employ the diffraction of light to observe a long air bubble confined in a solid rectangular channel filled with silicone oil. This setup, constituting a two-dimensional physical model of thin film drainage, allows us to analyze the influence of a SAW on the rate of thinning of the micron-thick liquid film separating the bubble and the solid substrate. The viscous penetration of the SAW into the liquid imposes a convective drift of mass, redistributing the fluid in the film against capillary resistance and producing a net drift of liquid out of the film. The rate of drainage of liquid from the film increases by one to several orders of magnitude in comparison to the rate of drainage due to the Laplace pressure of the bubble alone. The experimental findings agree well with a newly developed theory describing the SAW-enhanced drainage as a competition between the capillary flow and SAW-induced streaming.

DOI: [10.1103/PhysRevE.95.052803](https://doi.org/10.1103/PhysRevE.95.052803)

I. INTRODUCTION

The gradual thinning and subsequent breakdown of a liquid film is known as film drainage. Drainage contributes to a plethora of natural phenomena and technological procedures. Examples are the stability of suspensions [1], emulsions [2], and foam [3], the separation of particulates [4,5], the decay of tear films on our eyes [6], the efficiency of coating procedures [7], and the adhesion of bacteria onto a solid surface [8]. We report the dynamics and drainage of an intermediate 1 μm thick film of silicone oil between a bubble and a solid substrate—one of the simplest physical models for an intermediate liquid film in soft matter systems—under the influence of a propagating MHz-frequency Rayleigh surface acoustic wave (SAW) in the solid. The experiment is conducted by trapping a long bubble, whose dominant radius of curvature is $R \approx 50 \mu\text{m}$, in a microchannel filled with silicone oil. The experiment is designed to reduce the number of spatial dimensions of drainage by diminishing capillary contributions to film dynamics along the channel. Recent studies revealed that the viscous penetration of a propagating SAW into a neighboring film of liquid will generate a directional drift of mass that is sufficient for supporting a Landau-Levich dip-coating type flow [9] and dynamic wetting [10,11]. The conversion of the periodic motion of the SAW to a drift of liquid mass in the film via the advection of momentum is similar to mechanisms responsible for underwater oceanic currents. Oceanic currents may be invoked by gravity waves in deep and shallow water due to the wavy displacement of ocean free surface [12] and the viscous boundary layer appearing near the solid bottom [13], respectively. In this paper, we report that the viscous penetration of the SAW into the liquid may enhance the rate of drainage of the liquid film by several orders of magnitude compared to the rate of drainage under the influence of the Laplace pressure of the bubble alone. A model that accounts for both acoustic and capillary stresses in the liquid film trapped between a bubble and a solid is able

to account for the observations. Moreover, this study offers a first direct connection between high frequency acoustics and the drainage of liquid films.

The problem of a long bubble traveling through a circular capillary filled with liquid was first considered by Bretherton [14]. Wong *et al.* [15] extended the analysis to the case of a polygonal capillary. In particular, Wong *et al.* have shown that the thickness of the convex liquid film separating the bubble and the solid side of a rectangular capillary is determined by the capillary number $\text{Ca} \equiv \mu U_b / \gamma \ll 1$, where μ , U_b , and γ denote the shear viscosity in the liquid, velocity of the bubble motion through the capillary, and the surface tension of the liquid-air interface, respectively. According to Wong *et al.*, the geometry of the liquid film is determined by the balance between the drainage of liquid from the film due to Laplace pressure of the bubble and the influx of liquid due to motion of the bubble; specifically, far away from the front of the bubble, film thickness attains a maximum, where $h \sim \text{Ca}^{2/3}$, and two symmetric minima, where $h \sim \text{Ca}^{4/3}$. Chen *et al.* [16] verified the theoretical predictions of Ref. [15] for air bubbles in a square channel filled with a mixture of glycerol and water.

Furthermore, the drainage of liquid films and applications to the attachment of particles was intimately studied for over a century using various methods. Examples are found in measurements of the dynamic force between interacting particles in liquid using atomic force microscopy (AFM) [17,18] and the surface force apparatus (SFA) [19], measurements of the spatiotemporal variations of draining films using optical interference [20], and measurements of the time for coalescence of droplets using microfluidic platforms [21]. In particular, the collision of a bubble and a solid substrate entraps an intermediate convex film of liquid that slightly deforms the bubble; the film must drain before bubble-to-solid attachment may occur [22,23]. The drainage is usually forced by the Laplace pressure of the bubble and determined by viscous dissipation and the hydrodynamic constraints at the boundaries of the film, such as the presence of surface active species [24] or adsorbed polymers [25], for example. Typically, the slowest stage in the process of attachment is the drainage of

*manoro@technion.ac.il

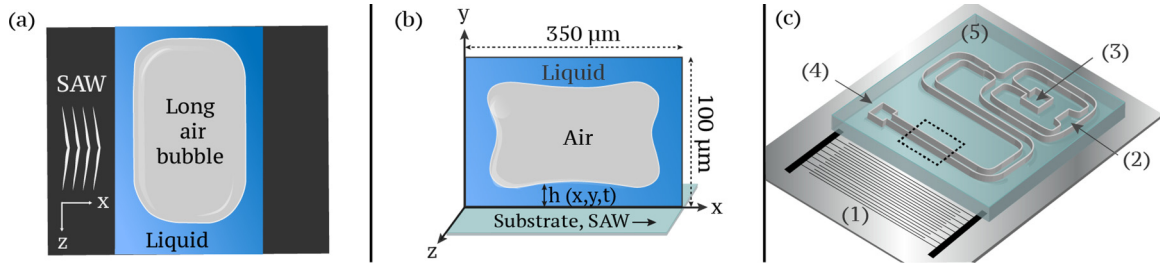


FIG. 1. (a) A sketch of a top view of an air bubble confined in a channel, (b) a sketch of the cross section of the channel and bubble (not to scale), and (c) a sketch of the experimental setup, where we show the (1) interdigital electrodes atop the piezoelectric substrate of the SAW actuator and the inlets for (2) oil, (3) air to the microchannel, and (4) the outlet of the fluids, fabricated within the (5) elastomer structure atop the actuator; the dashed square illustrates the area of observation.

the entrapped film, determining the statistical efficiency of the attachment process [26,27]. In the following, we scrutinize the dynamical response of the intermediate liquid film between a bubble and a solid to a MHz frequency SAW.

II. EXPERIMENTAL PROCEDURE

Our experimental setup, sketched in Fig. 1(c), consists of a channel fabricated in an elastomer of polydimethylsiloxane (PDMS), which is attached to an acoustic actuator using plasma (FEMTO PCCE, Diener Electronic). The thickness and width of the channel are 100 and 350 μm, respectively. The acoustic actuator is made of a piezoelectric lithium niobate substrate we pattern with aluminium-titanium interdigitated electrodes (IDTs). The coupling between the IDTs and the piezoelectric substrate is designed for the excitation of a Rayleigh SAW of a $f_{\text{SAW}} = 20$ MHz frequency. The motion at the surface of the lithium niobate substrate, supporting the SAW, comprises both longitudinal (along the surface) and transverse (normal to the surface) components. The velocity amplitudes of the components are related to the applied voltage. We excite the acoustic actuator using a signal generator (Rohde & Schwarz, SMB 100) and an amplifier (Rohde & Schwarz, BS2 5001-2). Using a scanning laser Doppler vibrometer (MSA-500, Polytec), we verified the SAW is a propagating wave and found the range of the transverse velocity amplitudes we generate at the solid surface of the acoustic actuator is $U_0 = 11\text{--}23$ cm/s. The measurements were taken near the IDT where the diffraction of the SAW is weak and before the SAW penetrates under the PDMS structure. Furthermore, the attenuation of the SAW is negligible on our microfluidic device when the SAW is propagating under air or under the intermediate liquid film in our experiment, possessing a thickness much smaller than the wavelength of the SAW (200 μm). However, the SAW attenuates in an appreciable manner as it travels under the PDMS structure, possessing a similar density to water. The attenuation of the SAW, propagating under the 1.5-mm-thick PDMS wall of the channel, yields a 40% decrease in the amplitude of the SAW at the solid surface [28]. Thus, the range of the transverse velocity amplitude of the substrate, supporting the SAW, is $U_{\text{SAW}} \approx 0.6U_0 = 6.6\text{--}14$ cm/s under the intermediate liquid film in the channel. In addition, the longitudinal velocity amplitude at the solid surface is smaller from its transverse counterpart by a factor of $\chi \approx 1.3$ for the Rayleigh SAW in

our experiment [29]. We further note that $U_{\text{SAW}} \sim 10$ cm/s corresponds to a SAW amplitude of about 1 nm, which is significantly smaller than the estimated thickness of the liquid film in the experiment.

In the course of each experiment, the microfluidic channel is first filled with silicone oil (Sigma-Aldrich silicone oils of viscosity $\nu = 50$ cSt, 100 cSt, or 500 cSt). Then an air bubble is deposited into the channel using syringe pumps (syringe pumps New Era pump system Inc., NE-100 and Chemyx Inc., Model Fusion 740 where used for silicone oil and air, respectively). The pumps generate pressure difference between inlet and outlet, which is open to the atmosphere, resulting in the gradual propagation of the bubble through the channel. We then turn off the pumps and open both inlets to the atmosphere, thus arresting the motion of the bubble. Since the bubble is much longer than the observation area, its specific stopping location is not relevant. We then illuminate the intermediate liquid film between the bubble and the solid substrate with a monochromatic light (wavelength of $\lambda = 436$ nm), using an upright microscope (Nikon, NE-I) equipped with a monochromatic filter (Chroma, 436/20X). The spatiotemporal variations in the image of the light fringes of equal chromatic order (FECO), captured using a monochromatic CCD camera (QIClick, QImaging), give the corresponding time and space variations in the thickness of the intermediate liquid film.

III. EXPERIMENTAL RESULTS

We employ the slow motion of a long bubble traveling through a rectangular channel filled with silicone oil in order to generate a two-dimensional model for an intermediate convex film of liquid between a bubble and a solid surface. Specifically, we exploit the fact that geometry of the film changes very slowly along the bubble [15] and consider only the flow in the cross-sectional plane of the channel. This two-dimensional physical model for drainage is particularly convenient for studying contributions from the linear front of a SAW, propagating along the spanwise direction (along the x axis) of the channel, as shown in Fig. 1.

A. Capillary drainage

After arresting the motion of the bubble in a 50 cSt oil and in the absence of the SAW in the substrate, we observe the gradual motion of the light interference fringes from the

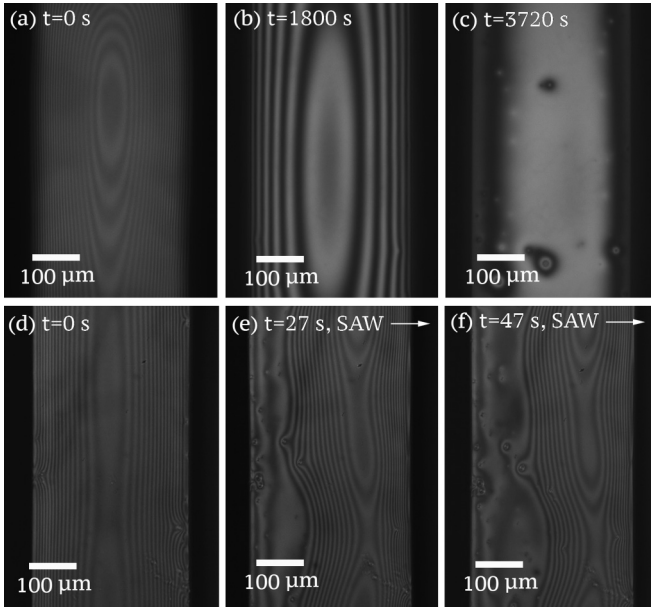


FIG. 2. A top view of the intermediate film of oil in terms of monochromatic light interference patterns, captured within the observation area in Fig. 1(c), for different times for 50 cSt oil in the absence (top row) and in the presence (bottom row) of a propagating SAW (along the arrow) of a measured velocity amplitude of $U_{\text{SAW}} = 0.11$ m/s at the solid surface.

center of the film to the side walls of the channel, shown at the top row in Fig. 2. The spatiotemporal variations in the light fringes indicate the thinning of the intermediate liquid film. The Laplace pressure drains the liquid from the film to the menisci at the sides of the channel [15], i.e., to the high-curvature segments of the surface of the bubble, sketched in Fig. 1(b) and shown as wide black stripes at the sides of the observation area in Fig. 2. For 50 cSt oil the image of fringes cease to change in time after about an hour. The center of the observation field becomes homogeneously bright with only one interference fringe separating the bright region from the menisci. The latter implies that the liquid film becomes mostly flat and that the difference in the liquid film thickness across the channel is less than $\lambda/2 = 218$ nm. No indication for the collapse of the film appeared in the fringe pattern approaching this state. This may be due to the presence of a negative Van der Waals force between the liquid-air interface and the liquid-solid interface, stabilizing the intermediate liquid film at small thicknesses [30]. Similar observations are captured for the other types of silicon oil, albeit the 100 cSt silicon oil appears to drain for 3 h and the 500 cSt oil appears to drain for 12 h.

These results, in the absence of SAW, are in a reasonable agreement with the analysis by Wong *et al.* [15], suggesting the spanwise rate of leakage of liquid from the intermediate film under a long bubble through each meniscus is given by

$$Q = \frac{C_1 \gamma h_c R}{3\mu L} \left(\frac{12V}{L^2} \right)^5, \quad (1)$$

where $C_1 \approx 1.2098$ and h_c , R , L , and $V \approx h_c L$ are, respectively, the characteristic thickness of the intermediate liquid film, the radius of curvature of the menisci at the corners of

the channel, the width of the liquid film, and the characteristic volume of liquid per unit length of the film. The typical time of drainage is then $T \sim V/2Q$, where the factor 2 in the denominator corresponds to the two menisci at each side of the film. We find that $T \approx 3.2 \times 10^3$ s for the 50 cSt oil, taking the characteristic thickness of the film to be $h_c \approx 1 \mu\text{m}$ and approximating $R \approx 50 \mu\text{m}$ (that is, half of the channel height). The typical time of drainage of the more viscous oils scales like the ratio of their shear viscosities to the one of the 50 cSt oil.

B. SAW-enhanced drainage

The presence of a SAW in the solid substrate alters the dynamics of the intermediate liquid film and the rate of drainage. The light interference fringes are pushed along the path of the propagating SAW, shown at the bottom row in Fig. 2. Moreover, the spatiotemporal variations in the light fringes indicate the bulk of liquid is pushed downstream in the direction of the SAW, while a flat plateau is formed upstream. The total number of interference fringes decreases in the course of experiment, suggesting that the liquid film flattens out on a time scale of minutes.

To further quantify the rate of drainage of liquid from the intermediate film, we captured the evolution of the light fringes. We then reconstructed the dynamics of the film geometry. Specifically, we sought for the evolution of the film thickness $h(x,t)$, where x is the spatial coordinate in the spanwise direction of the channel (sketched in Fig. 1), accepting $x = 0$ at the initial minimal film thickness at the right edge of the observation area (the area between the minimum thickness values of the film where we are able to accurately identify the light fringes), and t is time. Interference patterns carry information about the gradient of the film thickness, ∇h , rather than of h itself; thus, our reconstruction algorithm, described in the Appendix, yields the function $\Delta h(x,t) \equiv h(x,t) - h_0(t)$, where $h_0(t)$ is the minimal film thickness at the right edge of the observation area.

Typical results of the film geometry reconstruction are presented in Figs. 3 and 4. In Fig. 3, we demonstrate the effect of the SAW intensity on the film drainage: in the absence of SAW, the film geometry remains symmetric with respect to the center of the channel and the typical time of drainage is $\sim 10^3$ s (as shown in the top row of Fig. 3); whereas in the presence of SAW, the symmetry is lost and the typical time reduces to ~ 10 s (as shown in the middle and bottom rows of Fig. 3). Naturally, the rate of SAW-enhanced drainage decreases with viscosity of the silicone oil, as illustrated in Fig. 4.

IV. THEORY

Reconstructing the intermediate film geometry from the evolution of the interference patterns allows for the direct comparison of experiment and theory [9]. Following the analysis developed in Ref. [9], we scale the thickness of the film $h(t,x)$ using the viscous penetration length of the SAW into the liquid $\delta \equiv \sqrt{2\mu/\rho\omega}$, which is about $1 \mu\text{m}$ in our experiments, where ρ and $\omega \equiv 2\pi f_{\text{SAW}}$ are the density of the liquid and the angular frequency of the SAW, respectively. The characteristic length along the direction of drainage is further estimated from the radius of curvature of the

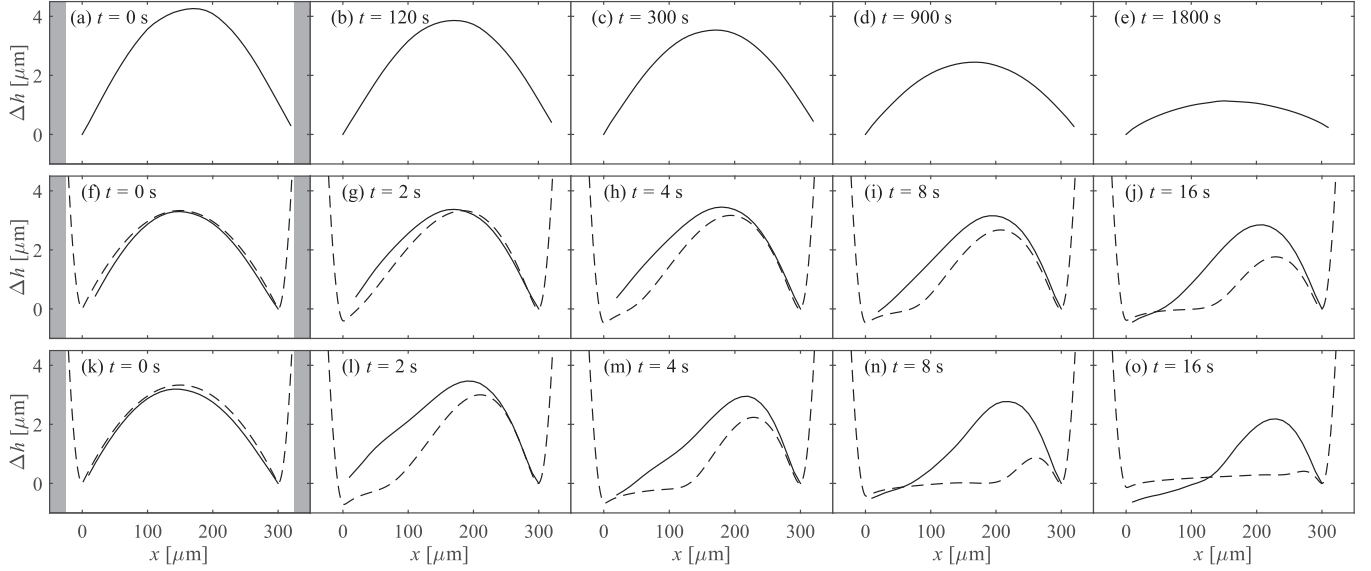


FIG. 3. Typical evolution of the thin-film geometry (Δh) in experiment (solid line) and in numerical computation (dashed line) for 50 cSt oil and (a–e) in the absence of SAW, (f–j) for $U_{\text{SAW}} = 6.3$ cm/s, and (k–o) for $U_{\text{SAW}} = 10$ cm/s. Gray stripes in the leftmost panels mark the position of the channel walls.

menisci at the corners of the channel, approximated to leading order as half the thickness of the channel, i.e., $R \approx 50$ μm . Furthermore, the drift velocity in the liquid film, invoked by the SAW, scales with $\text{Re}\chi U_{\text{SAW}}$, in which $\text{Re} \equiv \rho U_{\text{SAW}} \delta / \mu$, and the characteristic time associated with the acoustic forcing alone scales with $\delta / \text{Re}U$. The corresponding dimensionless evolution equation governing the flow in the intermediate film is

$$\frac{\partial h}{\partial t} + \frac{\partial}{\partial x} [h v(h)] + \frac{\partial}{\partial x} \left[\frac{h^3}{3\text{We}_s} \frac{\partial^3 h}{\partial x^3} \right] = 0, \quad (2)$$

where $\text{We}_s \equiv \epsilon^{-3} \chi \rho U_{\text{SAW}}^2 \delta / \gamma$ is the scaled acoustic Weber number, quantifying the ratio between the acoustic stress

$\chi \rho U_{\text{SAW}}^2$ and the capillary stresses γ / δ in the liquid film, and $\epsilon \equiv \sqrt{\delta / R} \ll 1$ is the lubrication parameter, quantifying the disparity of length scales in the film. In addition, the dimensionless drift velocity in Eq. (2) is

$$v(h) \equiv \frac{h \sinh(2h) - h \sin(h) + 2 \cos(h) \cosh(h)}{4h [\cos(2h) + \cosh(2h)]} - \frac{1}{4h}. \quad (3)$$

In the context of our experiment, the evolution Eq. (2) describes the drainage of the liquid film due to the combined action of both the applied SAW and capillary forces, represented by the second and the third terms on the left-hand side of the equation, respectively.

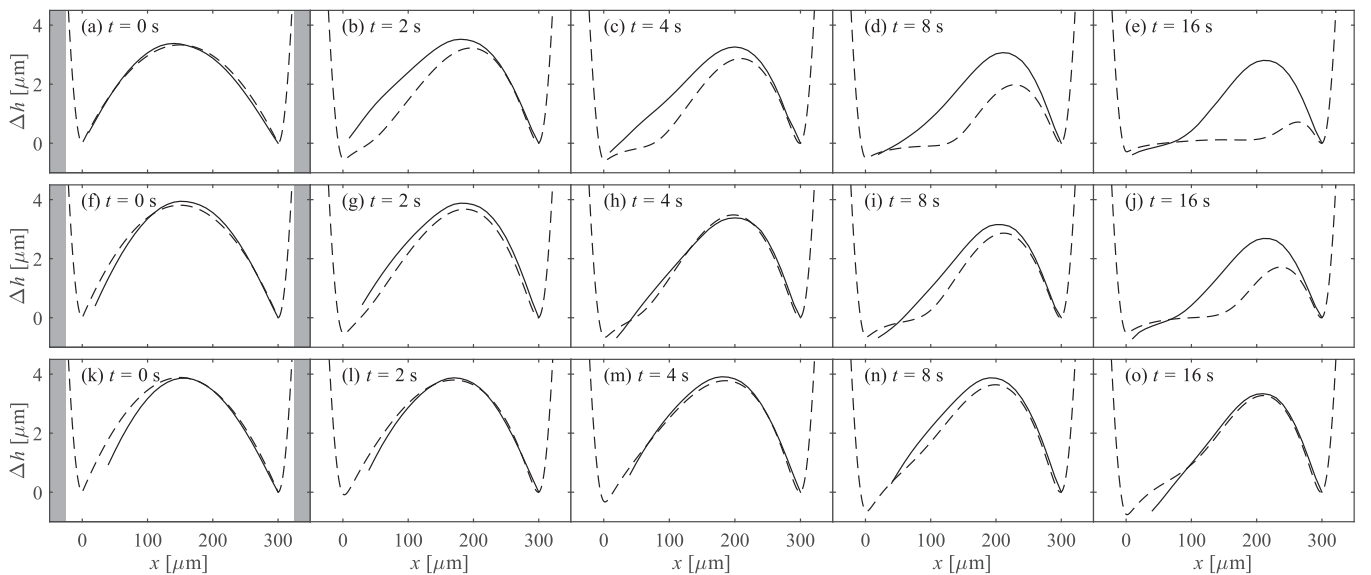


FIG. 4. Typical evolution of the thin-film geometry (Δh) in experiment (solid line) and in numerical computation (dashed line) for $U_{\text{SAW}} = 7.9$ cm/s and (a–e) for 50 cSt silicone oil, (f–j) 100 cSt silicone oil, and (k–o) for 500 cSt silicone oil. Gray stripes in the leftmost panels mark the position of the channel walls.

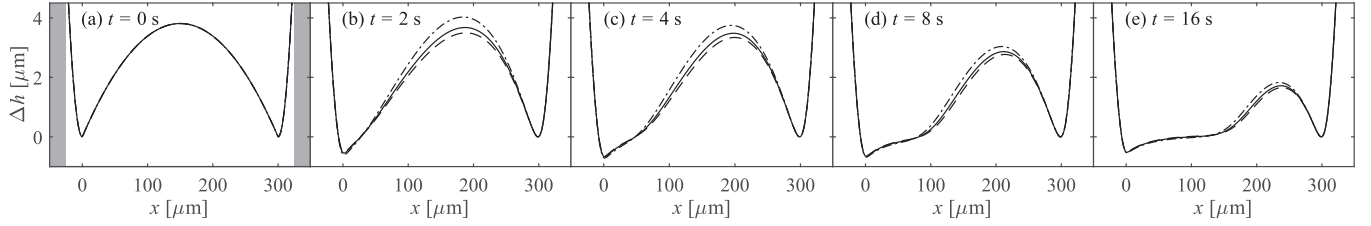


FIG. 5. Typical evolution of the thin-film geometry (Δh) in numerical computations for 100 cSt silicone oil, where $U_{SAW} = 7.9$ cm/s and $h_0(t = 0) = 0.1 \times \Delta h_{MAX}$ (solid line), $h_0(t = 0) = 0.05 \times \Delta h_{MAX}$ (dashed line), and $h_0(t = 0) = 0.2 \times \Delta h_{MAX}$ (dash-dot line). Gray stripes in the leftmost panels mark the position of the channel walls.

We solve the evolution Eq. (2) using the Newton-Kantorovich method [31], assuming that at $t = 0$ the film within the experimental observation area has a convex parabolic shape with a height similar to the one in the corresponding experiment, that is, $\Delta h_{MAX} \approx 3.7 \mu\text{m}$, $\Delta h_{MAX} \approx 3.0 \mu\text{m}$, and $\Delta h_{MAX} \approx 1.3 \mu\text{m}$ for the 50 cSt, 100 cSt, and 500 cSt oils, respectively. Outside of the observation area the initial curvature of the interface is $1/R$ and remaining at this value far away from the observation area, as shown in the leftmost panels of Figs. 3 and 4. Furthermore, the initial minimal thickness of the film, $h_0(t = 0)$, is not well defined using our experimental procedure. However, it was shown that far away from the front of the bubble, as in our experiment, it is small with respect to the initial maximum value of the film by a factor of the order of magnitude $O(\text{Ca}^{2/3}) \ll 1$ [15]. The characteristic capillary number in the experiments were $\text{Ca} = 3 \times 10^{-3}$, 6×10^{-3} , and 3×10^{-2} for the 50 cSt, 100 cSt, and 500 cSt oils, respectively. The initial minimum film thickness in the different experiments was smaller from the corresponding maximum value Δh_{MAX} by a numerical factor of approximately 2×10^{-2} , 3×10^{-2} , and 10^{-1} , respectively. We approximated $h_0(t = 0) \approx 0.1 \times \Delta h_{MAX}$ for ease of the numerical procedure since the numerical results appeared not sensitive to the exact value of h_0 within its physical range. In Fig. 5, we demonstrate that choosing $h_0(t = 0) \approx 0.05 \times \Delta h_{MAX}$ or $h_0(t = 0) \approx 0.2 \times \Delta h_{MAX}$ results in a change smaller than 11% in the overall dynamic thickness of the film $h(t > 0, x)$. The change was estimated using the infinity norm of the difference between (a) $h(t > 0, x)$ obtained for $h_0(t = 0) \approx 0.05 \times \Delta h_{MAX}$ and $h_0(t = 0) \approx 0.1 \times \Delta h_{MAX}$, and (b) $h(t > 0, x)$ obtained for $h_0(t = 0) \approx 0.1 \times \Delta h_{MAX}$ and $h_0(t = 0) \approx 0.2 \times \Delta h_{MAX}$.

The typical evolution of the film geometry in the course of the numerical computations is shown in Figs. 3 and 4. We observe a quantitative agreement between theory and experiment at the initial stages of the evolution, when the film deforms in a manner reminiscent of a kinematic wave. The latter observation implies that the spatiotemporal variation of the film geometry is compatible with the evolution Eq. (2), when the acoustic contribution, that is, the second term on the left-hand side of the equation, is dominant. The “kinematic” stage of the evolution lasts for about 5–15 s, depending on the SAW intensity and silicone oil viscosity.

At the later stage of the film evolution, we observe that the quantitative agreement between theory and experiment shifts to a qualitative agreement as the rate of drainage in the theory becomes significantly faster than in the experiment. We assume that the difference between theory and experiment at the later stage of drainage is due to the confinement of the draining liquid by the walls of the channel, which is not accounted for by the theory, shown in Figs. 3 and 4. In our theoretical model, we assume that the liquid drains into an infinite reservoir and avoid the contribution of the channel walls to the flow field. The shift from quantitative to qualitative agreement between theory and experiment is further shown in Fig. 6 in terms of the evolution of the apparent integral volume of liquid in the film; the apparent volume is the volume deduced from the light fringes in terms of

$$V = \int_{x=x_0}^{x=L} [h(x, t) - h_0(t)] dx. \quad (4)$$

Here L is the width of the observable area and x_0 corresponds to the leftmost point where $h(x, t) - h_0(t) \geq 0$.

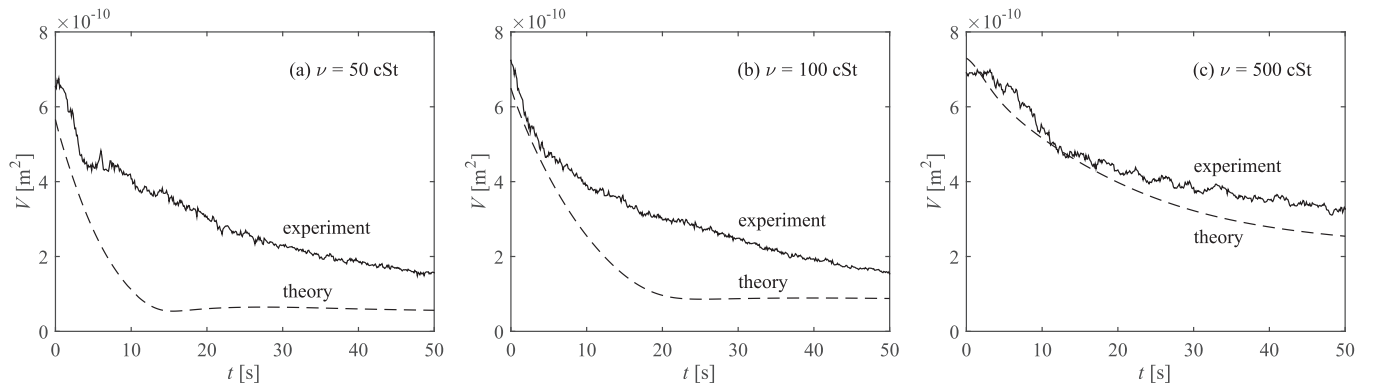


FIG. 6. Evolution of the apparent volume given by Eq. (4) in the experiment and numerical computation shown in Fig. (4) for $U_{SAW} = 7.9$ cm/s and (a) 50 cSt silicone oil, (b) 100 cSt silicone oil, and (c) 500 cSt silicone oil.

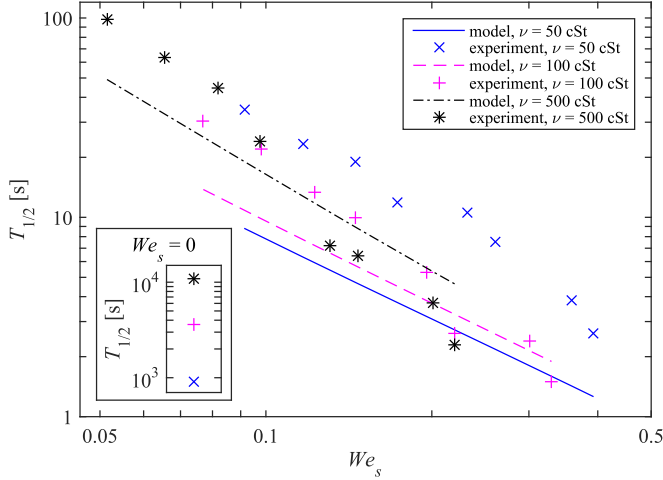


FIG. 7. Variations of the experimental and theoretical time interval corresponding to 50% decrease of the apparent liquid volume in the intermediate film, $T_{1/2}$, against the ratio between acoustic and capillary stresses in the liquid, We_s . In the absence of the SAW ($We_s = 0$), we measured $T_{1/2} = 900, 3600$, and $10\,800$ s for 50, 100, and 500 cSt oils, respectively, shown in the inset to the left.

V. DISCUSSION AND CONCLUSIONS

In this paper, we investigate a simple physical model for the drainage of a thin film. We employ a long air bubble, confined in a rectangular capillary, which is filled with silicone oil, as shown in Fig. 1. We use the diffraction of monochromatic light to monitor the spatiotemporal variations in the geometry of the intermediate liquid film between the bubble and the solid substrate of the channel. We further present experimental evidence showing that the presence of a SAW in the substrate may accelerate the rate of drainage of liquid from the film. In the absence of the SAW, the drainage is driven by the Laplace pressure of the bubble [15]. The flow of liquid out of the film is, however, limited by the film geometry: the region of the film adjacent to the menisci becomes exceedingly thin in time, resulting in a geometrical bottleneck, which is reducing the flow of liquid leaving the film. The theoretical time scale of drainage of a film of 50 cSt silicone oil is $T \approx 3.2 \times 10^3$ s; this result is compatible with the theoretical time scale, presented in the top rows of Figs. 2 and 3.

The presence of a SAW in the solid substrate may reduce the typical time of the drainage of the film by one to several orders of magnitude with respect the corresponding time scale in the absence of a SAW. The SAW supports a directional drift of liquid, which breaks the symmetry of the intermediate liquid film between the bubble and the solid, shown at the bottom row of Fig. 2, reducing the thinning of the liquid film near the downstream meniscus. Thus, the presence of the SAW excitation hinders the formation of the bottleneck region while supporting a drift of liquid out of the film, enhancing the drainage efficiency. This mechanism is summarized in Figs. 3, 4, and 6.

To further summarize our results, we demonstrate in Fig. 7 that the “half-life” of the liquid film, $T_{1/2}$, exhibits power-law scaling with We_s both in theory and in experiment. Specifically, we define $T_{1/2}$ as a time interval corresponding to a 50% decrease in the initial apparent volume of the

intermediate film. This measure of drainage time is particularly convenient since $T_{1/2}$ can be measured within the first 1–2 min of the experiment. Further, the estimation of the full drainage time is not well defined due to the exceedingly small drainage rates observed at the later stages of the film evolution. Both experimental and theoretical data presented in Fig. 7 exhibit a well-defined dependency on the Weber number We_s , suggesting that the drainage is indeed a result of the competition between the capillary flow and SAW-induced streaming. Moreover, the proximity of the data shown in Fig. 7 hints that there might be a universal function $T_{1/2}(We_s)$. At this stage, we are not able to identify this function and leave this question for future research. Finally, the “half-life” time $T_{1/2}$ of the liquid film measured in experiment and shown in Fig. 7 lies in the range of 1 to 100 s, depending on the viscosity of the draining oil and the intensity of the SAW. These values are one to four orders of magnitude smaller than the ones measured in the absence of the SAW.

ACKNOWLEDGMENT

We acknowledge support of this research by the Israel Science Foundation (ISF) under Grant No. 489/14.

A.H. and M.M. contributed equally to this work.

APPENDIX: VIDEO ANALYSIS PROCEDURE

In this appendix, we provide a detailed specification of the video analysis algorithm we developed to reconstruct the typical geometry of the liquid film observed in the experiment. We assume that the film geometry is homogeneous in the longitudinal direction of the channel and, thus, depends only on time t and the spatial coordinate in the spanwise direction of the channel x . Furthermore, recall that the interference patterns observed in the experiment and shown in Fig. 2 carry information about the gradient of the film thickness, $\partial_x h(x, t)$, rather than the film thickness $h(x, t)$ itself. That is, information contained within the interference patterns defines the film thickness up to an unknown constant $h_0(t)$ and our reconstruction algorithm yields certain function $\Delta h(x, t)$ defined as

$$\Delta h(x, t) \equiv h(x, t) - h_0(t). \quad (\text{A1})$$

Without loss of generality, we further assume that $h_0(t) = h(x = L, t)$; therefore, $\Delta h(x = L, t) = 0$, where L denotes the length of the observation area.

In the course of each experiment, we record the evolution of the interference patterns with the frame rate of 9 FPS. In order to obtain $\Delta h(x, t)$, for each of the frames we repeat the following steps:

- (1) We split the frame into a set of 40 pixel-wide horizontal stripes $S_k(i, j)$, $k = 1 \dots 26$.
- (2) For each of the stripes, we average the interference pattern along the vertical direction (that is, along the main axis of the channel),

$$\langle S_k \rangle(i) = \frac{1}{40} \sum_{j=1}^{40} S_k(i, j). \quad (\text{A2})$$

Averaging reduces the level of noise in the signal and allows us to consider a small set of 1D signals instead of the full 2D frame.

(3) We then crop the dark areas corresponding to the thick static menisci at the sides of the observation field (see Fig. 2 in the main text for an example). Specifically, we disregard the information beyond the points where the average of $\langle S_k \rangle$ over 10 neighboring pixels is less than $\frac{1}{2} \max_i \langle S_k \rangle(i)$.

(4) In order to further reduce the level of noise, we employ the wavelet filter based on the Mexican hat wavelet. In particular, we compute the wavelet image of $\langle S_k \rangle$ for oscillations with the period 3, 4, 6, 8, . . . 60 pixels using the function `cwtft` of the MATLAB programming language. We then compute the inverse wavelet transform using the function `icwtft` and obtain the set of filtered signals $F_k(i)$, $k = 1 \dots 26$.

(5) Troughs and crests of F_k correspond to dark and bright stripes of the original interference pattern. That is, to determine the position of the stripes, we should identify the extrema of F_k . We define by $E_k(i)$ the position of the i th extremum of F_k satisfying one of the following conditions:

$$E_k(i) - E_k(i - 1) > 15 \text{ pixels}, \quad (\text{A3a})$$

$$|F_k[E_k(i)] - F_k[E_k(i - 1)]| > 0.02 \max_i F_k(i). \quad (\text{A3b})$$

Note that conditions Eqs. (A3) are imposed in addition to the requirement that each point $E_k(i)$ is a minimum or maximum of $F_k(i)$. Conditions Eqs. (A3) are necessary to eliminate the parasitic oscillations missed by the wavelet filter.

(6) For the sake of simplicity we assume that $\Delta h(x, t)$ has a single maximum and this maximum corresponds to the point $E_k(i_{\max})$, such that the function

$$C_k(i) \equiv [E_k(i + 1) - E_k(i)][E_k(i) - E_k(i - 1)] \quad (\text{A4})$$

attains its maximum at $i = i_{\max}$. In other words, we seek for i_{\max} that yields the minimal possible curvature of the reconstructed film profile.

It is important to note that in reality $\Delta h(x, t)$ may have a number of extrema, for instance, due to the imperfections of the substrate (see Figs. 2(c) and 2(f) for an example). Since we cannot properly treat these imperfections, we seek for the maximum of C_k in the region devoid of imperfections where

$$E_k(i) < 1.2\bar{x}_{\max}. \quad (\text{A5})$$

Here \bar{x}_{\max} is the position of the maximum on the previous frame (we set $\bar{x}_{\max} = L$ if the previous frame is not available).

(7) We obtain the reconstructed film geometry $H_k(x)$ for each of the 26 stripes assuming that:

(a) the height difference between the two adjacent extrema $E_k(i)$ and $E_k(i - 1)$ is $\Delta h_0 = \lambda/4 = 109 \text{ nm}$ for $i < i_{\max} - 1$ and $-\Delta h_0 = -109 \text{ nm}$ for $i > i_{\max} + 1$;

(b) the height difference between $E_k(i_{\max})$ and $E_k(i_{\max} \pm 1)$ is $\pm \Delta h_0/2 = \pm 54.5 \text{ nm}$, respectively;

(c) since $\Delta h(x = L, t) = 0$ by definition, last detected extremum in each of the E_k corresponds to $\Delta h = 0$;

(d) the length of one pixel is $0.64 \mu\text{m}$.

(8) To suppress the effect of the inhomogeneities of interference patterns on the reconstructed film geometry, we discard four stripes yielding the highest values of $|E_k(i_{\max}) - \bar{x}_{\max}|$ [the average of $E_k(i_{\max})$ is used if the value of \bar{x}_{\max} is not available] and four more stripes yielding the highest values of $|N_k - \bar{N}|$, where N_k denotes the number of extrema detected in the stripe k and \bar{N} is the average number of extrema per stripe on the previous frame (average of N_k is used if the value of \bar{N} is not available).

(9) Since each of the remaining $H_k(x)$ is represented by a set of discrete points, we use cubic splines to interpolate all of the $H_k(x)$ to one spatial grid with the step of $10 \mu\text{m}$. Finally, we obtain $\Delta h(x, t)$ by means of averaging of the interpolated $H_k(x)$ over k . The typical result of the reconstruction procedure is shown in Figs. 3 and 4.

-
- [1] S. J. Langer, R. Klute, and H. H. Hahn, *Water Sci. Technol.* **30**, 129 (1994).
 - [2] R. Dagastine, R. Manica, S. Carnie, D. Chan, G. Stevens, and F. Grieser, *Science* **313**, 210 (2006).
 - [3] R. J. Pugh, *Adv. Colloid Int. Sci.* **64**, 67 (1996).
 - [4] F. Fu and Q. Wang, *J. Environ. Manage.* **92**, 407 (2011).
 - [5] J. Ralston, S. S. Dukhin, and N. A. Mishchuk, *Adv. Colloid Int. Sci.* **95**, 145 (2002).
 - [6] H. Wong, I. Fatt, and C. J. Radke, *J. Colloid Int. Sci.* **184**, 44 (1996).
 - [7] A. Sharma and G. Reiter, *J. Colloid Int. Sci.* **178**, 383 (1996).
 - [8] I. M. Marcus, M. Herzberg, S. L. Walker, and V. Freger, *Langmuir* **28**, 6396 (2012).
 - [9] M. Morozov and O. Manor, *J. Fluid Mech.* **810**, 307 (2017).
 - [10] A. R. Rezk, O. Manor, J. R. Friend, and L. Y. Yeo, *Nat. Commun.* **3**, 1167 (2012).
 - [11] A. R. Rezk, O. Manor, L. Y. Yeo, and J. R. Friend, *Proc. R. Soc. A* **470**, 20130765 (2014).
 - [12] G. G. Stokes, *Trans. Cambridge Philos. Soc.* **8**, 441 (1847).
 - [13] M. S. Longuet-Higgins, *Philos. Trans. Roy. Soc. London Ser. A* **245**, 535 (1953).
 - [14] F. P. Bretherton, *J. Fluid Mech.* **10**, 166 (1961).
 - [15] H. Wong, C. J. Radke, and S. Morris, *J. Fluid Mech.* **292**, 71 (1995).
 - [16] H. Chen, Q. Meng, and J. Li, *Appl. Phys. Lett.* **107**, 141608 (2015).
 - [17] H. Butt, B. Cappella, and M. Kappl, *Surf. Sci. Rep.* **59**, 1 (2005).
 - [18] R. Dagastine, G. Stevens, D. Chan, and F. Grieser, *J. Colloid Int. Sci.* **273**, 339 (2004).
 - [19] R. A. Pushkarova and R. G. Horn, *Langmuir* **24**, 8726 (2008).
 - [20] L. Fisher, E. Mitchell, D. Hewitt, J. Ralson, and J. Wolfe, *Colloids Surf.* **52**, 163 (1991).
 - [21] T. Krebs, K. Schroen, and R. Boom, *Soft Matter* **8**, 10650 (2012).
 - [22] W. A. Ducker, Z. Xu, and J. N. Israelachvili, *Langmuir* **10**, 3279 (1994).
 - [23] D. Y. C. Chan, E. Klaseboer, and R. Manica, *Soft Matter* **7**, 2235 (2011).

- [24] O. Manor, I. U. Vakarelski, X. Tang, S. J. O'shea, G. W. Stevens, F. Grieser, R. R. Dagastine, and D. Y. C. Chan, *Phys. Rev. Lett.* **101**, 024501 (2008).
- [25] O. Manor, T. Chau, G. Stevens, D. Y. C. Chan, F. Grieser, and R. Dagastine, *Langmuir* **28**, 4599 (2012).
- [26] A. S. C. Lawrence and O. S. Mills, *Discuss. Faraday Soc.* **18**, 98 (1954).
- [27] O. I. Vinogradova, *Langmuir* **11**, 2213 (1995).
- [28] R. M. Arzt, E. Salzmann, and K. Dransfeld, *Appl. Phys. Lett.* **10**, 165 (1967).
- [29] D. Royer and E. Dieulesaint, *Elastic Waves in Solids I* (Springer-Verlag, Berlin/Heidelberg, 1996).
- [30] J. Israelachvili, *Intermolecular and Surface Forces*, 3rd ed. (Elsevier Inc., New York, 2011).
- [31] J. P. Boyd, *Chebyshev and Fourier Spectral Methods* (Dover Publications, Mineola, NY, 2000).